

Spectral Analysis of Line Edge and Line Width Roughness using Wavelets

Ndubuisi G. Orji^{*a}

^aNational Institute of Standards and Technology
Gaithersburg, MD 20899

ABSTRACT

Although line edge and line width roughness (LER/LWR) have been key metrology challenges over the last 15 years, the advent of extreme-ultraviolet lithography (EUV) has increased the importance of its measurement and control. Lithographically printed features are now small enough that randomness in resist chemistry and in EUV photon during exposure results in noise in the patterned resist. This not only affects LER/LWR, but also defect density, including missing holes, shifted features, bridged lines and holes, and line shorts, among others.

Well before these stochastic induced roughness variations, there have existed various techniques to analyze roughness. These include power spectral density algorithms, methods to account for instrument bias in the data, identify and filter noise, and specify measurement uncertainty. In this work, analysis methods to evaluate LER and LWR spatial wavelengths, including partitioning and filtering out instrument errors, such as noise and probe effects are presented.

Our approach is based on wavelet-transform multiresolution analysis. One of the key advantages of wavelet transform over other signal processing techniques are its spatial-frequency localization and multi-scale view of the components of a profile or surface. This allows decomposing the data into different bands based on specific cutoffs and evaluating different approximations and surface-details at each cutoff band. *A priori* noise and probe information are used to determine and remove instrument-effects from the data, before calculating the unbiased roughness. The strength of this approach is that it is targeted only to specific spatial wavelengths that are associated with instrument noise or artifacts.

Keywords: Line edge roughness, Linewidth roughness, Wavelet Transform, Spectral Analysis.

1. INTRODUCTION

Although the effects of line edge and line width roughness on lithographically printed features have been studied for over twenty years[1,2], the introduction of extreme-ultraviolet lithography (EUVL) brings an added degree of importance and urgency. Earlier on, the motivation for studying LER was due to the non-scaling of edge roughness with shrinking device sizes. For EUVL, the randomness in resist chemistry and in EUV photon speed during exposure results in noise thereby increasing the occurrence and nature of LER [3]. This not only affects roughness, but also defect density, missing holes, shifted features, bridged lines and holes, and line shorts, among other effects[4-6].

Over the years, several measurement and analysis methods have been developed for LER[7], including those based on scanning electron microscopy (SEM)[8-10], atomic force microscopy (AFM)[11-14], optical critical dimension metrology[15], and small angle X-ray scattering[16]. Irrespective of technique, one of the most important aspects of LER analysis is the need to subtract noise[17-21] and instrument effects[22] from the data in order to get the real or unbiased roughness. This is because roughness is not an intrinsic parameter of the surface or line edge, but is affected by noise, evaluation length, pixel size, and instrument effects[23-25].

Here, we show the use of wavelet-based multiresolution analysis [26] for LER evaluation. Wavelets multiresolution analyses are windowing operations that divide the data into different-sized frequency components and are evaluated at a resolution that matches its scale. The strength of this techniques is that it is targeted to specific frequencies that are actually associated with instrument noise or artifacts. This prevents the removal of uncorrelated high frequency information that are not due to instrument noise.

*george.orji@nist.gov

Preprint

See published version at:

N. G. Orji "Spectral analysis of line edge and line width roughness using wavelets", Proc. SPIE 11611, Metrology, Inspection, and Process Control for Semiconductor Manufacturing XXXV, 1161116; <https://doi.org/10.1117/12.2584649>

1.1 Line Edge and Linewidth Roughness

The roughness of a line edge or width is defined as the deviation (or residuals) of the edge from normal, where the assumption is that the edge should be nominally straight. This deviation is defined in eq. 1,

$$\sigma_T^2 = \sigma_{true}^2 + \sigma_{noise}^2 \quad (1)$$

where σ_T is the total *rms* roughness, σ_{true} rms of the “true” roughness, and σ_{noise} is the rms of the noise component. σ_{noise} is mostly random and could be from different aspects of the measurement process. σ_{true} is defined in eq. 2, where x_k are the edge locations. Other analysis methods are frequency related parameters such as power spectral density (PSD), autocovariance function (ACF), and height-height covariance function (HHCF)[27].

$$\sigma^2 = \frac{1}{N} \sum_{k=1}^{N-1} (x_k)^2 \quad (2)$$

Although the three spectral methods listed above measure slightly different things, they are statistically similar, and all provide an estimate of the spectral content of the signal and can be derived from each other. The PSD describes the variance of a signal with respect to unit frequency and in its general form is defined as $S(f_j) = \frac{\Delta x}{N} |\sum_{k=1}^N x_k \exp[(2\pi i)jk/N]|^2$ at spatial frequency $f_j = j\Delta f$, where $j=1,2,\dots,N/2$, and Δx is spacing between points. The ACF is the covariance of a specific length of signal with a translated copy of itself as a function of the translation length, and is defined as $ACF_{k,k+h} = [(x_k - \bar{x})(x_{k+h} - \bar{x})]$, and HHCF measures the mean square difference of a signal from a translated copy of itself as a function of the translation length and is defined as $HHCF_{k+h} = [(x_k) - (x_{k+h})^2]$ [28]. σ^2 can also be expressed in terms of the PSD as $\sigma^2 = \frac{\Delta x}{N} \sum_{k=1}^N dx[x_k]^2$, which serves as a useful check on PSD computation. x_k are the edge locations. All three methods have been applied to LER/LWR analysis including the impact of etch processes on roughness and EUV resist LER[29,30]. Applicability of different types of spectral methods to semiconductor LER, their associated uncertainties, and suitable measurement protocols, are all areas of active research and standardization [31-35].

1.2 Wavelet Analysis

All wavelets have the general form shown in eq. 3 in discrete form (discrete wavelet transform- DWT), with its discrete scaling function defined in eq. 4, where j and k are integers. $\psi(x)$ is the main or “mother” wavelet and must satisfy the following conditions: the average values should be zero, $\int_{-\infty}^{\infty} \psi(x)dt = 0$; and the total power is finite, $\int_{-\infty}^{\infty} |\psi(x)|^2 dt < \infty$. A series of basis functions can be obtained by translating and dilating $\psi(x)$. At higher frequencies, dilation of the mother wavelet is small, which provides good scale (time) resolution but weak frequency resolution, making it suitable for fast changing details. However, dilation is larger at low resolution, which results in weak scale (time) resolution but good frequency resolution. This time-frequency resolution is one of the most important attributes of wavelets, and have resulted in their use in image compression, time series and multiresolution analyses among others. For an overview of wavelets including their theory, applications, and implementations, see references [26,36,37].

$$\psi_{j,k}[x] = 2^{j/2} \psi(2^j x - k) \quad (3)$$

$$\phi_{j,k}[x] = 2^{j/2} \phi(2^j x - k) \quad (4)$$

Wavelets have also been used extensively for surface roughness analysis, especially in bandwidth filtering and multiresolution analysis[38-42]. Part of the appeal in using wavelets for surface metrology is the ability to decompose the signal into roughness at different scales. Unlike Fourier transform methods, where all the frequencies are treated with equal resolution in both space and frequency domains, the variable size windowing approach of wavelets allows large windows to be used when low frequency information is needed and smaller windows when high frequency information is needed. Chen et al. [38] and Fu et al.[39] have used this method to evaluate the roughness of turned surfaces. Others have proposed ways to use different aspects of wavelets to evaluate edge roughness[43-45]. Here, we apply this wavelet multiresolution analysis and filtering to unbiased LER evaluation.

2. MULTIREOLUTION ANALYSIS USING WAVELETS

Broadly speaking, multiresolution filtering is a way to use the windowing capabilities of wavelets to separate the surface into different frequency domains before analysis. There are two broad categories of wavelets, orthogonal and biorthogonal wavelets[26]. Although both can be used for multiresolution analysis, biorthogonal wavelets are preferred due to their symmetry. The DWT (eq. 3) operates on scales and positions based on powers of two (dyadic sampling) and leads to a more compact, efficient implementation of wavelets.

The main components of multiresolution analysis are decomposition and reconstruction. Decomposition involves sequentially dividing the data into different components at different resolutions. Each decomposition produces two signals, referred to as approximation and details. The approximation or details signal (depending on the analysis being performed) is decomposed again. Each decomposition is called a level, and the total number of levels or decompositions will depend on the analysis being performed, the frequencies of interest and the selected filters. Consider a signal $y = f(x)$, where $f(x)$ is an edge segment or a series of linewidths. The wavelet decomposition of such a signal will be the linear combination of the approximations and details as shown in eq. 5, where A and D represent the approximations and details at all levels.

$$f(x) = Af((x)) + Df((x)) \quad (5)$$

In practice, an efficient implementation of multiresolution analysis is done using filter banks[46], where the data is sliced into different components using a series of filters depending on the frequencies of interest. To explicitly link wavelets and filters, in eqs. 6 and 7, we express $\psi(x)$ (wavelet equation) and $\phi(x)$ (scaling function) as:

$$\phi(x) = \sum_k h_0(k) \sqrt{2} \phi(2x - k) \quad (6)$$

$$\psi(x) = \sum_k h_1(k) \sqrt{2} \psi(2x - k) \quad (7)$$

where $\sum_k h_0(k) = 1$, $\sum_k (-1)^k h_0(k) = 0$, and h_0 and h_1 are low pass and high pass filters. Applying the functions shown in eqs. 6 and 7 at each level in eq. 5, we get eq. 8, where $A_{j,k}$ and $D_{j,k}$ are coefficients.

$$f(x) = \sum_k A_{j,k} \phi_{j,k}(x) + \sum_k D_{j,k} \psi_{j,k}(x) \quad (8)$$

Figure 1 shows an implementation of discrete wavelet transform using recursive filter bank. At each level, two filters are applied to the signal, a low pass filter to obtain the approximation and a high-pass filter for the details. This operation produces a new dataset with twice the size of the original input. This leads to a fair amount of redundant data, and loss of efficiency. To solve this problem, the output is down-sampled by 2, and the even-number output is used for the next filter sequence. This process is schematically shown in figure 2.

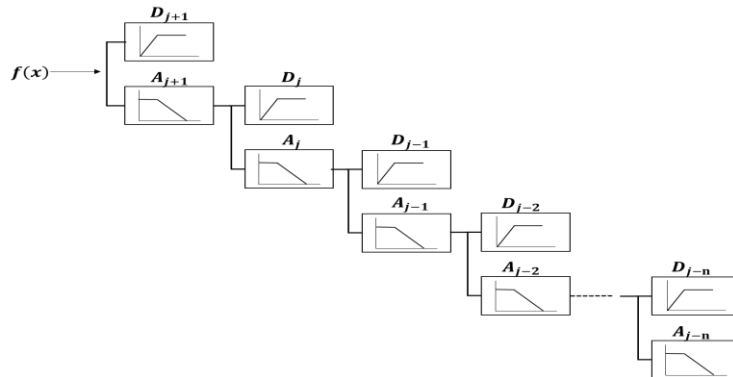


Figure 1: Diagram of implementation of discrete wavelet transform using recursive filter bank shown with just the approximation and details coefficients at each decomposition level.

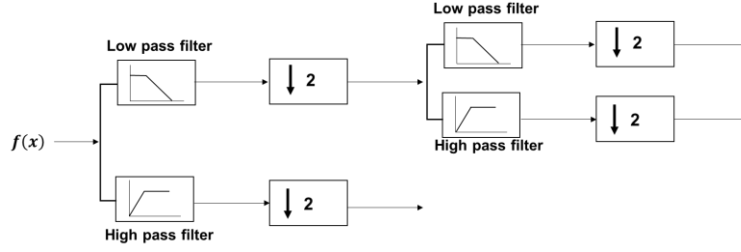


Figure 2: Sequential application of low and high pass filters and dyadic down-sampling. Each low pass and high pass operation produce twice the original data. Down-sampling by 2 ($\downarrow 2$), reduces the data size to the original level.

3. ANALYSIS

3.1 LER Measurement

All the data shown below were acquired from a critical dimension atomic force microscope (CD-AFM)[11,14,47]. This analysis can also be done using SEM data, albeit with different data processing and edge extraction methods. We measured a 2 μm segment of an EUV resist pattern, using a post tip with a width of 16.5 nm \pm 1 nm ($k=1$). The tip uncertainty was obtained using transmission electron microscopy based qualification methods, see refs [48] and [49] for more details. The noise level of the instrument was evaluated using the “Disable scan method” described by Azarnouche et al.[50], where the scan along the length of the feature is disabled and the variance of the acquired signal is the noise. As Azarnouche et al[50] pointed out, for AFMs, the sources of this noise could be due to tip stiffness[51,52] and/or the tip/sample interaction[53]. In addition, we also evaluated the instrument for systematic deviation that could affect the low frequency components of the signal. Figure 3 shows a profile of the edge roughness used in the analysis. Although the descriptions in the previous section are in terms of frequency, since our data have a strong spatial interpretation, we will use “wavelength” (inverse of frequency) where appropriate.

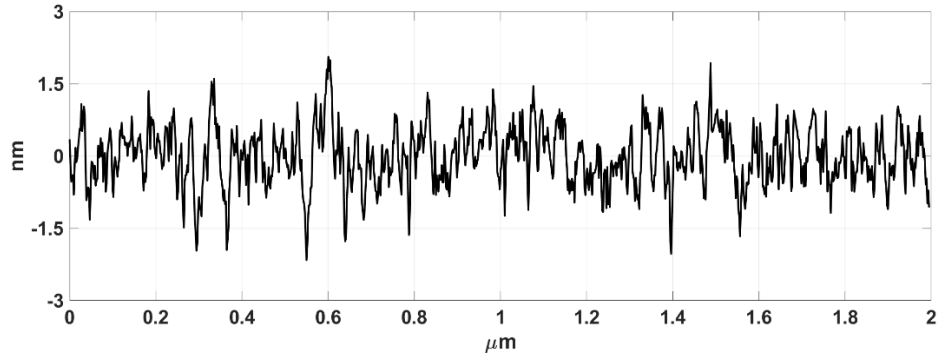


Figure 3. Extracted edge profile from CD-AFM data.

We selected a filter from the Biorthogonal family of wavelets – Biorthogonal-5.5, which is symmetric, has linear phase and can be implemented using a fast algorithm[26]. The two numbers indicate the number of vanishing moments for deconstruction and reconstruction. A wavelet of n vanishing moment is orthogonal to polynomials of degree $n-1$. Generally, the higher the vanishing moments, the more complex signals a wavelet basis can evaluate (see Daubechies[26] and Strang and Nguyen[46] for additional information). Figure 4 shows the impulse response functions for the lowpass and high-pass decomposition filters. Applying the low and high pass filtering sequence shown in figure 2, we obtain the multiresolution decomposition for the edge profile in figure 3. This is shown in figure 5 for a 7-level decomposition, where the profiles in 5(a) are the approximations and those in 5(b) are the details. The numbers next to the profiles are the wavelength cutoffs. For the approximations (figure 5(a)), these values are the low pass filter wavelength cutoff starting from 0.004 nm. The corresponding values for the details (figure 5(b)) are the bandpass wavelength cutoff range for each

profile. Figure 6 shows the roughness at different levels of the decomposition and is obtained by applying a high-pass filter at each wavelength level.

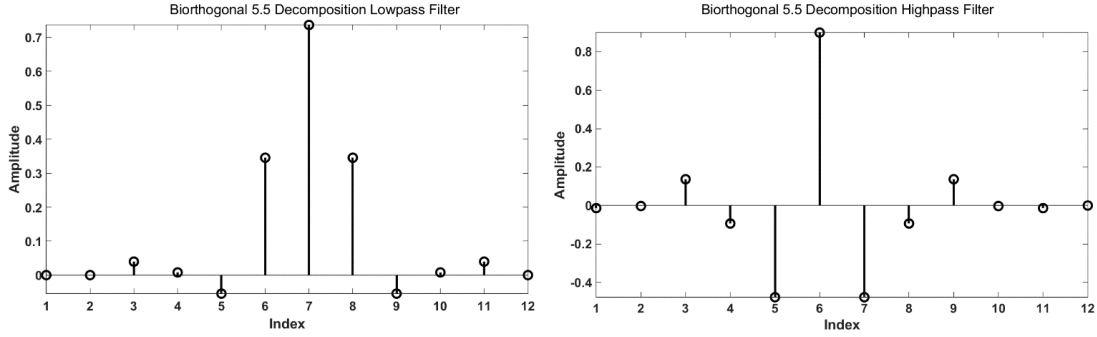


Figure 4: Biorthogonal-5.5 impulse response filters for decomposition. (a) lowpass and (b) high-pass

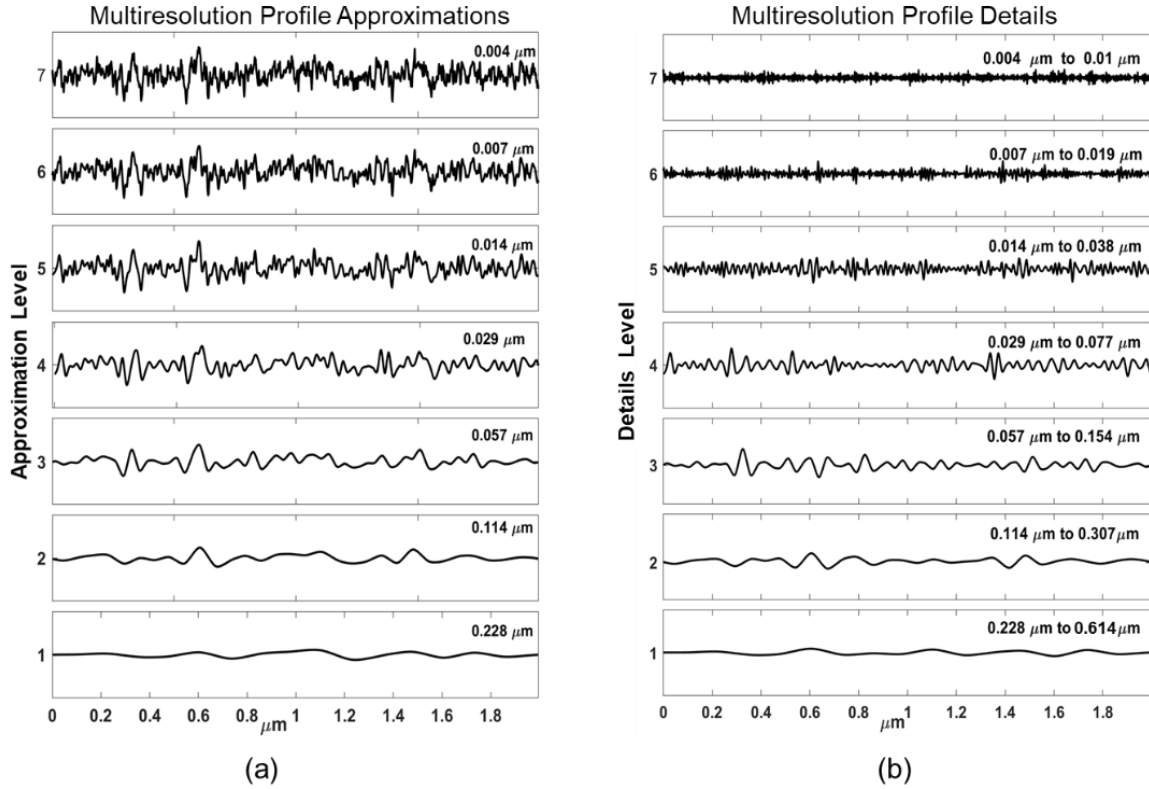


Figure 5: (a) Approximation profiles. The numbers next to the profiles represent the low pass filter cutoff for the analysis. (b) Details profiles from multiresolution Wavelet decomposition of a line edge profiles. The numbers next to the profiles represent the bandpass filter cutoff range used for the analysis. The Wavelet filter is Biorthogonal-5.5.

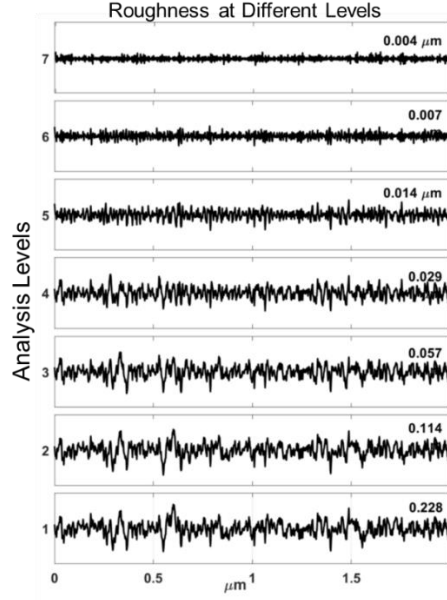


Figure 6: Roughness at different wavelength levels after applying the wavelet transform. The values beside each profile represent the high-pass filter cutoff.

3.2 Noise Removal and Unbiased LER

To get unbiased edge roughness, we have to remove systematic and random noise from the data. From previous analysis [54,55] we know that the noise starts at below $0.029 \mu\text{m}$ wavelength cutoff, meaning that we have to remove this portion of the data before roughness analysis. This is based on a combination of the random noise, tip size, data spacing, and probe dynamics [51,52,56]. This is done by setting all the coefficients below $0.029 \mu\text{m}$ wavelength cutoff to zero and reconstructing the profile. Figure 7 shows the impulse response function for the high-pass and low pass Biorthogonal-5.5 wavelets used. Figure 8 shows the reconstruction sequence analogous to the decomposition sequence shown in figure 2. The notable difference being that coefficients denoted as noise are set to zero. The signal at each level is up-sampled by 2, and zeros are inserted at odd-indexed locations, then convolved with the corresponding filter before moving to the next level. The original and reconstructed profiles are overlaid in figure 9. Using eq. 2, the original line edge profile yields a roughness of $\approx 1.54 \text{ nm}$, while the reconstructed (unbiased) roughness produces a value of $\approx 1.36 \text{ nm}$, a difference of more than 11 %.

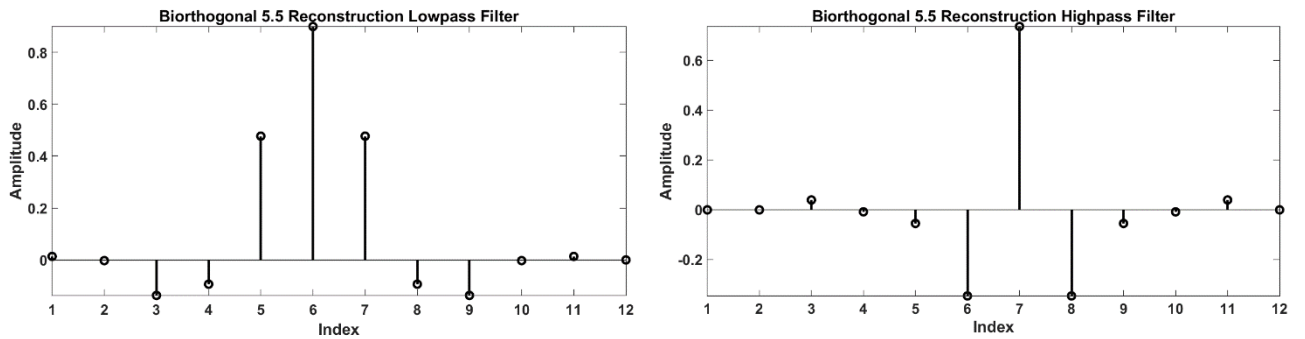


Figure 7 Biorthogonal-5.5 impulse response filters for reconstruction (a) lowpass and (b) high-pass.

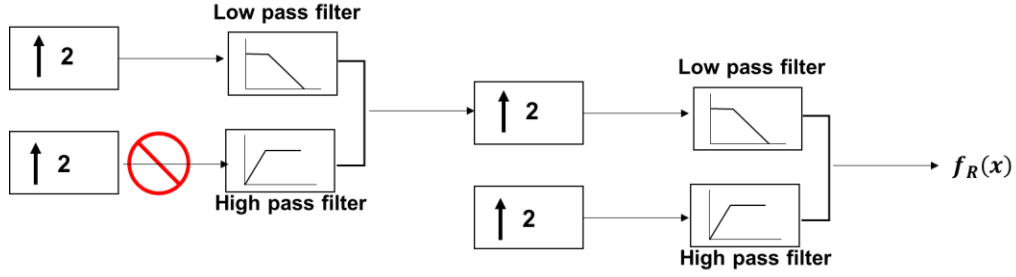


Figure 8: Reconstruction by sequential application of up-sampling by 2 ($\uparrow 2$) and convolving with low and high pass filters. Unneeded coefficients are set to zero.

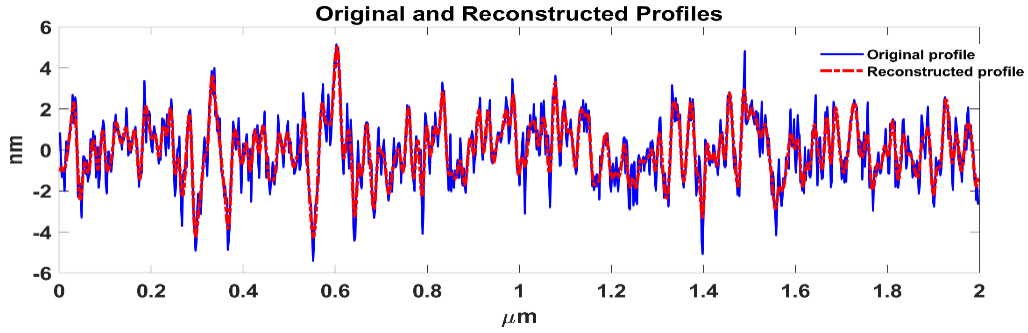


Figure 9: Original and reconstructed profile. The reconstructed profile is the unbiased roughness profile after removing noise effects.

3.3 Signal Averaging

One method used to obtain unbiased roughness is by aligning and averaging a series of profiles collected from the same location. This produces a profile of the same edge, but with reduced noise. We compared the roughness of the average of ten profiles obtained from repeated measurements at the same location and a reconstructed profile from the same ensemble. The average edge profiles are shown in figure 10, plotted with their average. Applying the decomposition sequence to one of the profiles we get the approximation, details, and roughness profiles shown in figure 11.

The cutoff wavelengths in figure 11 are the same with those in figures 4 and 5 because the data have the same spacing and were sampled based on Nyquist criterion. Since the data is from the same instrument, the noise behavior is the same as the previous data and shows up at $\approx 0.019 \mu\text{m}$ and below. Setting levels 6 and 7 to zero during the reconstruction, we get the data shown in figure 12, plotted with the original profile. The reconstructed profile has an rms value of $\approx 1.41 \text{ nm}$. The average profile has an rms value of $\approx 1.6 \text{ nm}$, calculated from the PSD shown in figure 12. So, more noise was removed by multiresolution analysis than simple averaging. This is consistent with we have seen in previous analysis, at least for averages of up to 20 lines. An important takeaway from the PSD in figure 13 is that 10 profiles are not enough to suppress the noise from LER data. Additionally, is not clear if the reduction from simple averaging is consistent with the noise level of the instrument. The benefit of using the multiresolution analysis approach is that the noise removal is targeted specifically to the relevant wavelengths.

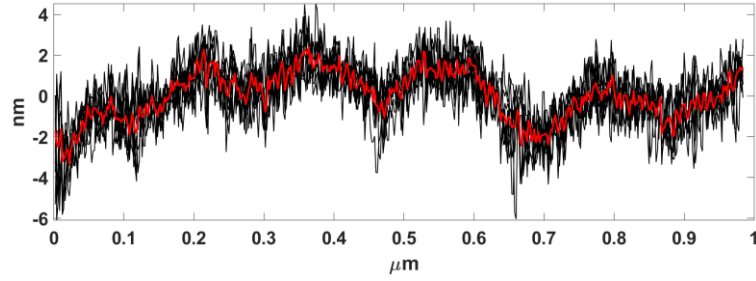


Figure 10: Edge profiles taken from the same location. The red profile in the middle is an average of 10 profiles.

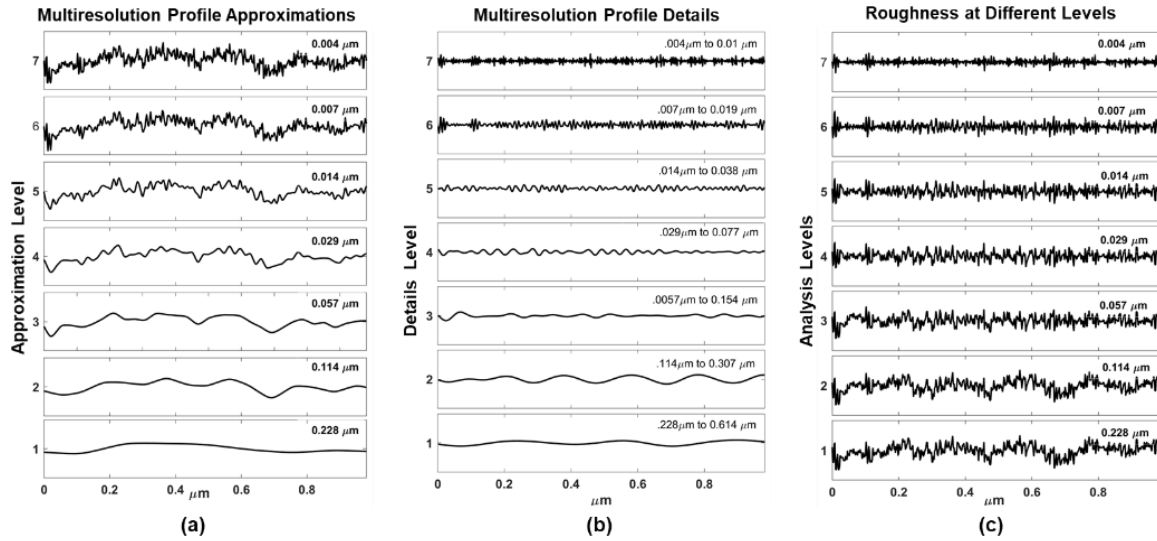


Figure 11: (a) Approximation, (b) decomposition, and (c) roughness profiles for a seven-level decomposition.

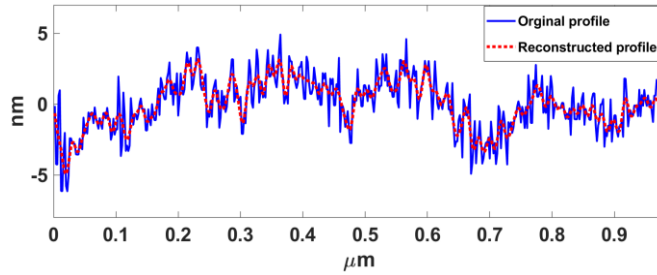


Figure 12: Original and reconstructed profile of one of the profiles plotted in figure 10. The reconstructed profile is the unbiased roughness profile after removing noise effects.

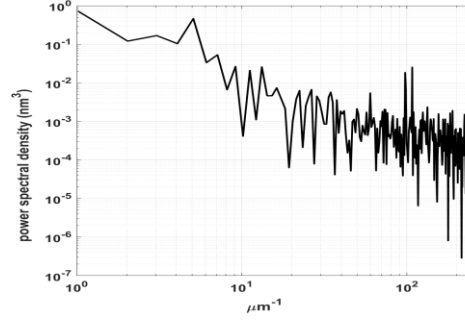


Figure 13: PSD plot of the averaged profile shown in figure 10

4. SUMMARY AND DISCUSSION

We showed the application of wavelet based multiresolution analysis to LER/LWR analysis, specifically for removing instrument effects from the signal and obtaining an unbiased roughness value. Although CD-AFM data is used in this analysis, the data could be from any instrument that can measure LER. Each instrument will have different noise characteristics and edge detection data requirements. A key consideration is not to do any type of image smoothing before edge detection.

Although the cutoffs used for this analysis are based on sampling of the Nyquist frequencies, the procedure allows the flexibility to select specific cutoffs depending on *a priori* knowledge. The lowest wavelength cutoff used in the analysis were determined by multiples of the Nyquist sampling criterion, and then doubled (and rounded up) at each level. The instrument noise level is affected by the random noise, tip size, data spacing, and probe dynamics. Although the data spacing is 2 nm, the probe has a width of 16.5 nm \pm 1 nm, ensuring that the extreme high frequency limit (Nyquist criterion: = $\frac{1}{2}$ (sampling interval) of the measurement is suppressed by mechanical filtering[57]. Although the tip-width is technically not a noise source, it is the dominant factor in the high-frequency roll-off of the instrument transfer function. So if using an AFM, careful consideration should be given to tip-size selection. Other factors are the pixel spacing, noise from the “disable scan method” (derived lateral component), and tip bending [51,58,59]. Our estimate of the cutoff wavelength was \approx 18.2 nm. If additional information about the noise spatial wavelength is not available, the tip width should be used. Note that the noise level is not 18.2 nm, rather an estimate of what the spatial wavelength cutoff should be. Determining the smallest cutoff wavelength is important and will depend on a good understanding of instrument characteristics.

The bandpass ranges shown in 5(b) and 11(b), are selected such that $Df((x))_L = \begin{cases} x, & \lambda_{Af(x)} \leq \lambda_{Df(x)} < \lambda_q \\ 0, & \text{for all other wavelengths} \end{cases}$, where $Df((x))_L$ is

the details component from eq. 6, $\lambda_{Af(x)_L}$ is the wavelength at the same approximation level and λ_q is the bandpass wavelength limit for that level. This explains why the approximation and details profiles start to converge after a certain wavelength cutoff. Simply put, for the data shown in figure 5, after a wavelength cutoff of 0.114 μ m there isn't much higher frequency detail to extract from the signal. The roughness profiles in figure 6 could be thought of as residuals of the approximation profile at each level with respect to the original profile, the details in figure 5(b) are obtained solely from the approximation profile for that level using a bandpass filter that starts from the approximation cutoff wavelength.

More broadly speaking, different frequencies of roughness in an edge pattern can be attributed to processing conditions or material[34], here the ability to separate and evaluate that information at a resolution that is matched to the scale is helpful. When compared with Fourier based techniques, wavelets provide both time (or spatial) and frequency information, whereas Fourier based spectral analysis where only time (or spatial) averaging frequency information without indicating the location of a specific frequency event. This is evident in figures 5-7, where we can say not only what the dominant frequencies are, but what the profiles look like. Compare this with the PSD shown in figure 13, where the less dominant frequencies appear as noise. In addition, roughness is a non-stationary signal, and contains many time-varying and transitory characteristics such as drift, trends, spikes and other components that represent specific attributes of the measurement system, and in some cases mathe signal.

5. CONCLUSION

We showed the application of wavelet based multiresolution analysis to LER/LWR analysis. The above results show the multiresolution analysis could be used to remove unwanted data from LER/LWR profiles to obtain an unbiased value and is based on our knowledge of which frequencies (or wavelengths) are relevant for our system. We view multiresolution analysis as a complementary technique to Fourier based methods, due to the multi-scaled view of roughness they provide and the flexibility of their implementation. Decomposing the data into approximations and details using a filter bank and sampled at specific frequencies allows the removal of unwanted portions of the signal, before reconstruction. The need to obtain unbiased roughness data that closely represents the features being measured is good application of wavelet multiresolution analysis. Although there are a wide range of noise filtering and smoothing algorithms, the specificity of multiresolution analysis makes them ideal for LER analysis.

REFERENCES

- [1] Oldiges, P., et al. Modeling line edge roughness effects in sub 100 nanometer gate length devices. *SISPD 2000* 131 (2000).
- [2] Diaz, C.H., et al., An experimentally validated analytical model for gate line-edge roughness (LER) effects on technology scaling. *IEEE Electron device letters*, 22(6), 287 (2001).
- [3] Neisser, M. and Levinson, H. Projecting EUV photo-speeds for future logic nodes. *Proc. SPIE* 11323, (2020). <https://doi.org/10.1117/12.2551311>
- [4] De Bisschop, P., Stochastic printing failures in extreme ultraviolet lithography. *J. Micro/Nanolith. MEMS MOEMS*, 17(4), 041011 (2018). <https://doi.org/10.1117/1.JMM.17.4.041011>
- [5] Bunday, B.D., et al. High volume manufacturing metrology needs at and beyond the 5 nm node. *Proc. SPIE* 11611, 116110F (2021).
- [6] *International Roadmap for Devices and Systems (IRDS) Metrology Chapter*. 2021 ed., IEEE, Piscataway, NJ, (2021).
- [7] Ma, Z. and Seiler, D.G., *Metrology and Diagnostic Techniques for Nanoelectronics*. CRC Press, (2017).
- [8] Bunday, B.D., et al., Determination of optimal parameters for CD-SEM measurement of line edge roughness. *Proc. SPIE*, 5375, 515 (2004). <http://dx.doi.org/10.1117/12.535926>
- [9] Bunday, B.D., et al. CD-SEM measurement line-edge roughness test patterns for 193-nm lithography. *Proc. SPIE* 5038, 674 (2003).
- [10] Yamaguchi, A., et al. Characterization of line-edge roughness in resist patterns and estimations of its effect on device performance. *Proc. SPIE* 5038, 689 (2003).
- [11] Orji, N.G., et al., Line edge roughness metrology using atomic force microscopes. *Meas. Sci. Technol.*, 16(11), 2147 (2005).
- [12] Fouchier, M., et al., An atomic force microscopy-based method for line edge roughness measurement. *J. Appl. Phys.*, 113(10), 104903 (2013).
- [13] Kizu, R., et al., Line edge roughness measurement on vertical sidewall for reference metrology using a metrological tilting atomic force microscope. *J. Micro/Nanolith. MEMS MOEMS*, 19(1), 014003 (2020).
- [14] Orji, N.G. and Dixon, R.G., 3D-AFM Measurements for Semiconductor Structures and Devices, in *Metrology and Diagnostic Techniques for Nanoelectronics*. 109, Pan Stanford, NY. (2017).
- [15] Dixit, D.J., et al., Sensitivity analysis and line edge roughness determination of 28-nm pitch silicon fins using Mueller matrix spectroscopic ellipsometry-based optical critical dimension metrology. *J. Micro/Nanolith. MEMS MOEMS*, 14(3), 031208 (2015).
- [16] Reche, J., et al. Application of PSD for the extraction of programmed line roughness from SAXS. *Proc. SPIE* 10959, (2019). <https://doi.org/10.1117/12.2514919>
- [17] Villarrubia, J. and Bunday, B., *Unbiased estimation of linewidth roughness*. *Proc. SPIE*. Vol. 5752. SPIE, (2005).
- [18] Liang, A., et al. Unbiased roughness measurements: the key to better etch performance. *Proc. SPIE* 10585, 9 (2018).
- [19] Lorusso, G.F., et al., Unbiased roughness measurements: Subtracting out SEM effects, part 2. *J. Vac. Sci. Technol. B*, 36(6), 06J503 (2018).

- [20] Papaveros, G., et al. Allowable SEM noise for unbiased LER measurement. *Proc. SPIE* 10585, 105851W (2018).
- [21] Mack, C., et al. Unbiased roughness measurements: subtracting out SEM effects, part 3. *Proc. SPIE* 10959, (2019). <https://doi.org/10.1117/12.2515898>
- [22] Bunday, B.D. and Mack, C.A. Influence of metrology error in measurement of line edge roughness power spectral density. *Proc. SPIE* (2014). <http://dx.doi.org/10.1117/12.2047100>
- [23] Orji, N.G., et al., Metrology for the next generation of semiconductor devices. *Nature Electronics*, 1(10), 532 (2018). <https://doi.org/10.1038/s41928-018-0150-9>
- [24] Vorburger, T.V., et al., In the rough. *Optical Engineering Magazine*, 31 (2002). <https://doi.org/10.1117/2.5200203.0008>
- [25] Orji, N.G., et al., Measurement traceability and quality assurance in a nanomanufacturing environment. *Proc. SPIE* vol. 7405, 740505 (2009).
- [26] Daubechies, I., *Ten lectures on wavelets*. SIAM, (1992).
- [27] Constantoudis, V., et al., Line edge roughness and critical dimension variation: Fractal characterization and comparison using model functions. *J. Vac. Sci. Technol. B*, 22(4), 1974 (2004). <https://avs.scitation.org/doi/abs/10.1116/1.1776561>
- [28] Mack, C.A., Biases and uncertainties in the use of autocovariance and height–height covariance functions to characterize roughness. *J. Vac. Sci. Technol. B*, 34(6), 06K701 (2016).
- [29] Mack, C.A., Reducing roughness in extreme ultraviolet lithography. *J. Micro/Nanolith. MEMS MOEMS*, 17(4), 041006 (2018).
- [30] Bizen, D., et al., CD metrology for EUV resist using high-voltage CD-SEM: shrinkage, image sharpness, repeatability, and line edge roughness. *J. Micro/Nanolith. MEMS MOEMS*, 18(3), 034004 (2019).
- [31] Constantoudis, V., et al., Line edge roughness metrology: recent challenges and advances toward more complete and accurate measurements. *J. Micro/Nanolith. MEMS MOEMS*, 17(4), 041014 (2018). <https://doi.org/10.1117/1.JMM.17.4.041014>
- [32] Lorusso, G.F., et al., Need for LWR metrology standardization: the imec roughness protocol. *J. Micro/Nanolith. MEMS MOEMS*, 17(4), (2018). <https://doi.org/10.1117/1.JMM.17.4.041009>
- [33] Hiraiwa, A. and Nishida, A., Statistical-noise effect on discrete power spectrum of line-edge and line-width roughness. *J. Vac. Sci. Technol. B*, 28(6), 1132 (2010). <https://avs.scitation.org/doi/abs/10.1116/1.3499647>
- [34] Cutler, C., et al., Pattern roughness analysis using power spectral density: application and impact in photoresist formulation. *Journal of Micro/Nanopatterning, Materials, and Metrology*, 20(1), 010901 (2021).
- [35] Semi, *Test Method for Evaluation of Line-Edge Roughness and Linewidth Roughness*, Milpitas, CA, (Semiconductor Equipment and Materials 2013).
- [36] Burrus, C.S., Introduction to wavelets and wavelet transforms: a primer. *Englewood Cliffs*, (1997).
- [37] Jawerth, B. and Sweldens, W., An overview of wavelet based multiresolution analyses. *SIAM review*, 36(3), 377 (1994).
- [38] Chen, X., et al., Multi-scale analysis of engineering surfaces. *International J. Mach. Tools and Manuf.*, 35(2), 231 (1995).
- [39] Fu, S., et al., Engineering surface analysis with different wavelet bases. *J. Manuf. Sci. Eng.*, 125(4), 844 (2003).
- [40] Jiang, X., et al., Application of the lifting wavelet to rough surfaces. *Precision Engineering*, 25(2), 83 (2001).
- [41] Raja, J., et al., Recent advances in separation of roughness, waviness and form. *Precision Engineering*, 26(2), 222 (2002).
- [42] Muralikrishnan, B. and Raja, J., *Computational surface and roundness metrology*. Springer-Verlag, London, (2008).
- [43] Li, H.-B., et al., Study on parameters of line edge roughness based on wavelet theory. *J. Harbin Instit. Technol.*, 04 (2006).
- [44] Wang, F. and Li, N., Multi-Scale Analysis of Line Edge Roughness Based on Wavelet Transform. *Microscopy and Microanalysis*, 16(S2), 474 (2010).
- [45] Zhao, X., et al., Analysis method for nanometer-scale line edge roughness based on stationary wavelet transforms. *Nanotechnol. & Prec. Engin.*, 7(2), 147 (2009).
- [46] Strang, G. and Nguyen, T., *Wavelets and filter banks*. SIAM, (1996).
- [47] Dixon, R., et al., Spatial dimensions in atomic force microscopy: Instruments, effects, and measurements. *Ultramicroscopy*, 194, 199 (2018). <https://doi.org/10.1016/j.ultramic.2018.08.011>

- [48] Orji, N.G., et al., TEM calibration methods for critical dimension standards, *Proc. SPIE* vol. 6518, 651810 (2007)
- [49] Orji, N.G., et al., Tip characterization method using multi-feature characterizer for CD-AFM. *Ultramicroscopy*, 162, 25 (2016). <http://dx.doi.org/10.1016/j.ultramic.2015.12.003>
- [50] Azarnouche, L., et al., Unbiased line width roughness measurements with critical dimension scanning electron microscopy and critical dimension atomic force microscopy. *J. Appl. Phys.*, 111(8), 084318 (2012).
- [51] Ukraintsev, V.A., et al., Distributed force probe bending model of critical dimension atomic force microscopy bias. *J. Micro/Nanolith. MEMS MOEMS*, 12(2), (2013).
- [52] Dixon, R., et al., Interactions of higher order tip effects in critical dimension-AFM linewidth metrology. *J. Vac. Sci. Technol. B*, 33(3), 031806 (2015). <https://doi.org/10.1116/1.4919090>
- [53] Orji, N.G., et al. Toward accurate feature shape metrology. *Proc. SPIE* 6922, 692208 (2008).
- [54] Orji, N.G., et al., Contour metrology using critical dimension atomic force microscopy. *Proc. SPIE* vol. 8324, 83240U (2016).
- [55] Orji, N.G., et al. Strategies for nanoscale contour metrology using critical dimension atomic force microscopy. *Proc. SPIE* 8105, 810505 (2011).
- [56] Dixon, R., et al., Effects of lateral tip control in CD-AFM width metrology. *Meas. Sci. Technol.*, 25(9), 094003 (2014).
- [57] Orji, N.G., et al., Progress on implementation of a CD-AFM-based reference measurement system, *Proc. SPIE* vol. 6152, p. 61520OJ (2006).
- [58] Choi, J., et al., Evaluation of carbon nanotube probes in critical dimension atomic force microscopes. *J. Micro/Nanolith. MEMS MOEMS*, 15(3), (2016). <https://doi.org/10.1117/1.Jmm.15.3.034005>
- [59] Park, B., et al. Application of carbon nanotube probes in a critical dimension atomic force microscope. *Proc. SPIE* 6518, 651819 (2007).